IEEE Access
Multidisciplinary | Rapid Review | Open Access Journal

Received 13 December 2022, accepted 23 December 2022, date of publication 28 December 2022,
date of current version 10 January 2023.

Digital Object Identifier 10.1109/ACCESS.2022.3232843

RESEARCH ARTICLE

Novel Rotor Structure Employing Large Flux Barrier and Disproportional Airgap for Enhancing Efficiency of IPMSM Adopting Concentrated Winding Structure

XIANJI TAO[1], MASATSUGU TAKEMOTO[2], (Member, IEEE), REN TSUNATA[2], (Member, IEEE), AND SATOSHI OGASAWARA[1], (Senior Member, IEEE)
[1]Graduate School of Information and Technology, Hokkaido University, Sapporo, Hokkaido 060-0814, Japan
[2]Graduate School of Natural Science and Technology, Okayama University, Kita-ku, Okayama 700-8530, Japan

Corresponding author: Masatsugu Takemoto (mtakemoto@okayama-u.ac.jp)

This work was supported by the Japan Science and Technology Agency (JST) SPRING under Grant JPMJSP2119.

ABSTRACT Interior permanent magnetic synchronous motors (IPMSMs) adopting concentrated windings have been widely used in industrial applications. To reduce operating costs, it is an important issue to enhance the efficiency of an IPMSM as much as possible while maintaining manufacturing costs. In general, an IPMSM used for an industrial application always operates in a specific operating area according to the required load. Therefore, this paper has two purposes. The first purpose is to propose a novel rotor structure which can enhance efficiency at the target wide-speed middle-torque operating area without additional manufacturing costs. The second purpose is to clarify the design method for a suitable rotor structure depending on its target operating area. Reducing losses is the key to enhancing efficiency. This paper first examines the effects of adopting large flux barriers and a disproportional airgap on copper and iron losses, and clarifies their merits and respective high-efficiency operating areas. Furthermore, to take advantage of the two rotor structures, a novel rotor structure which employs both large flux barriers and a disproportional airgap has been proposed. 2D-FEM (Finite-Element Method) is used for discussion first, and a prototype machine is manufactured to verify the 2D-FEM results. Both 2D-FEM and experimental results show that the proposed rotor structure can enhance the efficiency of an IPMSM most effectively at the target operating area. Moreover, for a low-speed high-torque operating area, adopting only large flux barriers is most suitable. And for a high-speed low-torque operating area, adopting only a disproportional airgap is most suitable.

INDEX TERMS IPMSM, concentrated winding structure, high efficiency, flux barrier, disproportional airgap.

I. INTRODUCTION

Interior permanent magnet synchronous motors (IPMSMs) have been widely used in industrial applications for their outstanding characteristics, such as simple structure, high power density, wide speed range, and good speed control, especially for their high efficiency [1], [2], [3], [4], [5]. Moreover, because industrial applications are generally cost-sensitive, concentrated winding structure has been widely adopted to cut manufacturing costs and use limited space effectively [6], [7], [8]. At the same time, to reduce operating costs, it is also an important issue to enhance the efficiency of an IPMSM as much as possible while maintaining manufacturing costs, which is the main purpose of this paper.

In general, an IPMSM used for an industrial application always operates in a specific operating area according to the required load. And to enhance efficiency effectively,

The associate editor coordinating the review of this manuscript and approving it for publication was Tao Wang.

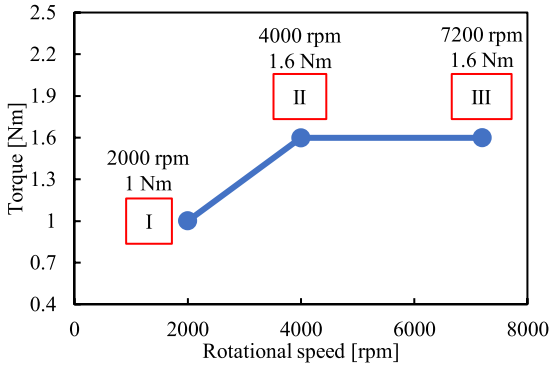

(a) Target operating area

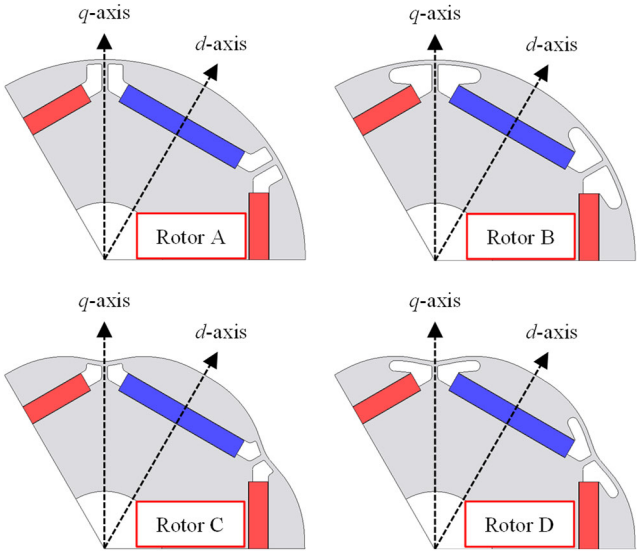

(b) A brief overview of the four rotor structures

FIGURE 1. Target operating area and a brief overview of the four rotor structures discussed in this paper.

IPMSMs should be designed suitably depending on their target operating areas. This paper particularly concerned with efficiency in the wide-speed middle-torque operating area. Fig. 1(a) shows the operating area and target operating line in this paper. The target operating point line can be considered typical operating points for a motor used in an air conditioner compressor. In most cases, the operating point moves on the target operating line depending on the temperature difference between indoor and outdoor. And a maximum torque of 2.5 Nm at 7200 rpm is also required for extreme temperature differences. To facilitate further comparison, three operating points, designated as point I (2000 rpm, 1 Nm), II (4000 rpm, 1.6 Nm), and III (7200 rpm, 1.6 Nm), respectively, have been selected for this paper.

Reducing losses is the key to enhancing efficiency. The major losses of an IPMSM can be divided into copper and iron losses without considering mechanical loss. Moreover, because the magnetoresistance of air is much larger than that of ferromagnetic material, the magnetic flux path of an IPMSM can be changed by changing the shape of flux barriers and its airgap, which can affect losses significantly. In previous studies, the torque can be increased by changing the shape of flux barriers, which are mentioned in [9], [10], and [11]. Additionally, all these studies show that an appropriate flux barrier design can reduce torque ripple. And the effect of asymmetry flux barriers examples on torque and its ripple is also discussed in [9] and [11]. Moreover, in [12], the magnetic flux leakage in the rotor iron bridges is eliminated with a rotor employing novel non-magnetic wedges. By adopting this structure, torque can also be increased because the non-magnetic wedges have a similar effect to flux barriers. At the same time, adopting a disproportional airgap can reduce the harmonic components and make the magnetic field distribution in the airgap closer to a sine wave. The study [13] uses a rotor with a disproportional airgap that shows core losses and torque ripple can be reduced while the torque decreases, and dynamic stability has also been enhanced. Similarly, in [14], cogging torque is reduced by adopting a disproportional airgap. However, contrary in study [13], the torque in this study increases. The previous studies have mentioned rotor structures with large flux barriers and disproportional airgaps, and these studies also demonstrate that both the two rotor structures can change average torque and suppress torque ripple depending on their shape. However, their advantages from the standpoint of enhancing efficiency compared with other rotor structures have not been illustrated in detail. Moreover, the efficiency of the wide-speed middle-torque operating area shown in Fig. 1(a) has been scarcely investigated. Therefore, this paper has two purposes. The first purpose is to propose a novel rotor structure which can enhance efficiency at the target wide-speed middle-torque operating area without additional manufacturing costs. The second purpose is to clarify the design method for a suitable rotor structure depending on its target operating area.

For easy understanding, Fig. 1(b) provides a brief overview of the four rotor structures discussed in this paper. And the stator structure has not been changed in this paper. Rotor A, which has minimum flux barriers on q-axis magnetic flux path, is the basic rotor structure in this paper. Rotor B adopts large flux barriers on q-axis magnetic flux which can concentrate the magnetic flux of permanent magnets (PMs) on d-axis while suppressing q-axis magnetic flux. Rotor C adopts a disproportional airgap on q-axis magnetic flux path which can suppress q-axis magnetic flux and dq-axis harmonic magnetic flux. Rotor D is the proposed rotor structure in this paper, which employs both large flux barriers and a disproportional airgap to take advantage of both Rotors B and C. This paper first examines the effects of adopting large flux barriers and a disproportional airgap on the utilization ratio of magnetic flux generated by PMs, the dimension of q-axis magnetic flux path, and the proportion of harmonic iron loss components, before examining their effects on copper and iron losses. 2D-FEM (Finite-Element Method) is used for discussion first. And 2D-FEM results show that the efficiency of Rotor B is higher than that

of Rotor C at operating point II because the copper loss of Rotor B is reduced effectively. While the efficiency of Rotor C is higher than that of Rotor B at operating point III because the iron loss of Rotor C is reduced effectively. For the target operating line, either copper or iron losses should be reduced because neither copper nor iron losses are dominant. Therefore, Rotor D is proposed to achieve the most efficient model on the target operating area by taking advantage of both Rotors B and C and realized a tradeoff between copper and iron losses to minimize total loss.

A prototype machine is manufactured to verify the 2D-FEM results. Both 2D-FEM and experimental results show that the proposed rotor structure, which employs both large flux barriers and a disproportional airgap, can enhance the efficiency of an IPMSM most effectively at the target operating area. Moreover, for a low-speed high-torque operating area, adopting only large flux barriers is most suitable. And for a high-speed low-torque operating area, adopting only a disproportional airgap is most suitable.

The structure of this paper is as follows. Chapter II proposes the structure of the basic model. The advantages of the rotor adopting large flux barriers and the rotor adopting a disproportional airgap are illuminated in Chapter III and IV, respectively. In Chapter V, a novel rotor structure employing both large flux barriers and a disproportional airgap has been proposed to take advantage of the two rotor structures mentioned above. Finally, experimental verification is shown in chapter VI.

In addition, the copper and iron losses can be changed by changing the load current and its phase angle to minimize total loss. And this control strategy is called maximum efficiency control for an IPMSM. Unless otherwise specified, the maximum efficiency control strategy is used throughout this paper. Moreover, 2D-FEA is executed by using an electromagnetic field simulator (JMAG-designer ver. 20.0, JSOL Co., Ltd.).

TABLE 1. Design specification.

Design specification	
Stator core outer diameter [mm]	90
Stator core inner diameter [mm]	43
Airgap length [mm]	0.6
Stacked length [mm]	48
Magnet weight [g]	61.29
Slots number	9
Poles number	6

II. BASIC STRUCTURE OF IPMSM

The design specification for the IPMSM in this paper are shown in Table 1. The stator core outer diameter is 90 mm, and the stacked length is 48 mm. The magnet weight is 61.29 g. It should be noted that the weight and shape of the magnets used for rotors have not been changed in this paper to avoid increasing manufacturing costs. As mentioned in the previous chapter, concentrated winding structure has been used to cut manufacturing costs. Therefore, to achieve high efficiency, a 6-pole/9-slot combination has been adopted, which ensures that the inverter's maximum drive frequency is less than or equal to 400 Hz at 7200 rpm while considering the balance of copper and iron losses at the target operating line [15], [16].

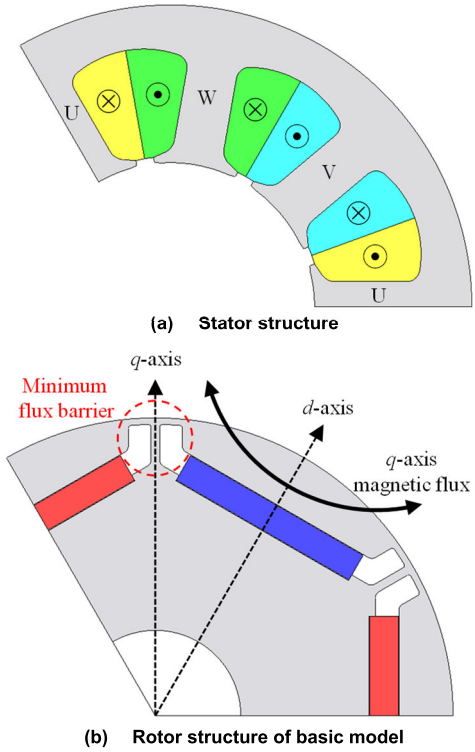

FIGURE 2. Stator and rotor structure of basic model.

Fig. 2 shows the stator and the rotor structure of the basic model, respectively. To evaluate the difference in efficiency performance of IPMSMs caused by different rotor structures, as shown in Fig. 2(a), the stator structure has not been changed in this paper. Fig. 2(b) shows the rotor structure of the basic model, and this basic model is called Model A. The manufacturing costs and difficulty of Model A are determined by an IPMSM used for a mass-produced air-conditioner compressor. There are minimum flux barriers on q-axis magnetic flux path which can ensure that no magnetic flux short circuits in the rotor core. As a result, this rotor structure can generate reluctance torque easily for its wide q-axis magnetic flux path. Moreover, only the one-third models of the stator and rotor are shown in Fig. 2. The full model can be regarded as a repetition of three one-third models. As a result, the magnetic forces generated in the radial direction can be cancelled and no unbalanced magnetic force generates in the 6-pole/9-slot combination.

III. INVESTIGATION OF ROTOR STRUCTURE WHICH FOCUSES ON MINIMIZING COPPER LOSS

Fig. 3 shows the rotor structure and its sketch for Model B, respectively. As shown in Fig. 3(a), compared with Model A, there are large flux barrier on q-axis magnetic flux path

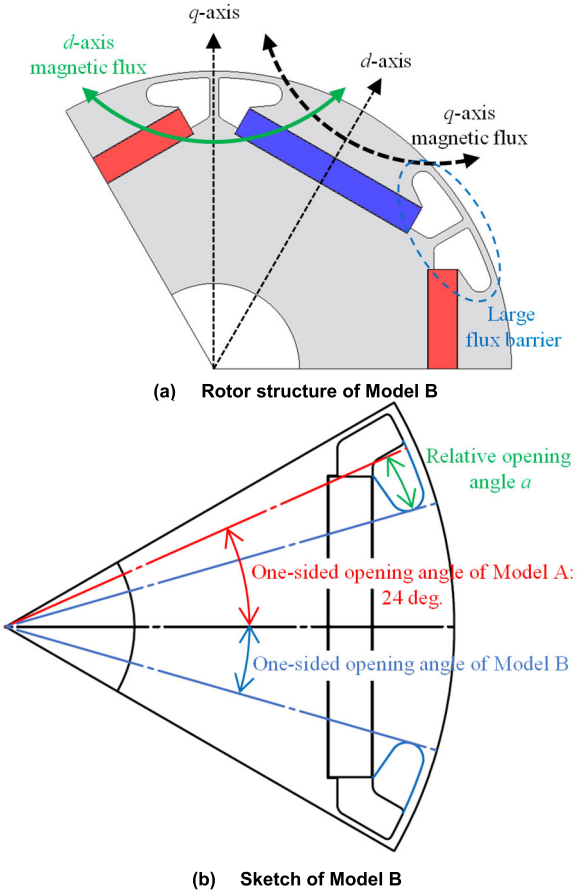

FIGURE 3. Rotor structure and its sketch for Model B.

to concentrate the magnetic flux of PMs on d-axis while suppressing q-axis magnetic flux. In other words, the characteristic of Model B is that it can generate a larger PM magnetic flux density in airgap. As a result, Model B is a rotor structure which can generate magnetic torque easier. Moreover, the differences of Model B from Model A are marked by the blue lines in Fig. 3(b). The one-side opening angle of Model A is approximately 24 deg. To evaluate the influence of the opening angular on copper loss, angle a is defined as the relative opening angle between Models A and B.

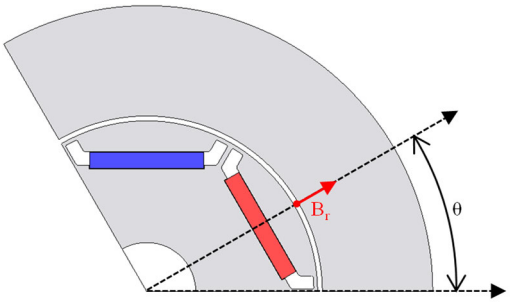

FIGURE 4. Observation point of PM magnetic flux density in the airgap.

Fig. 4 shows the observation point of PM magnetic flux density in the airgap. To eliminate the influence of stator slots, there are no slots in the stator. At the observation point indicated by the red dot located in center of the airgap, PM magnetic flux density (B_r) in radial direction is observed with the variation of mechanical angle θ.

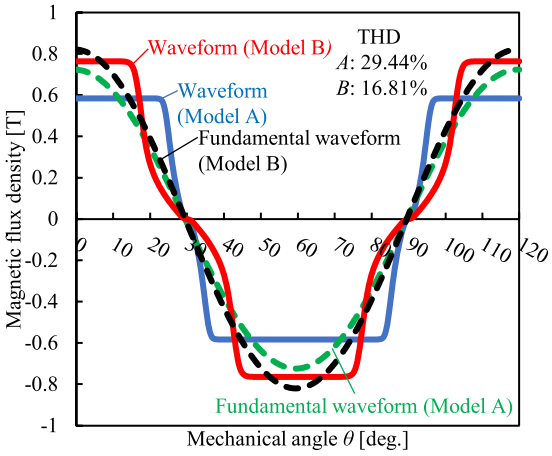

FIGURE 5. Magnetic flux density waveforms and their fundamental waveforms observed in the airgap.

Fig. 5 shows the magnetic flux density waveforms and their fundamental waveforms of Models A and B ($a = 8$ deg.) observed in the airgap. The waveform of Model A is close to a rectangular wave. Compared with Model A, PM magnetic flux density has been concentrated on the d-axis in Model B ($a = 8$ deg.) by the large flux barriers. As a result, the fundamental wave amplitude of magnetic flux density in Model B ($a = 8$ deg.) is 0.820 T, which is 13.32% larger than the 0.724 T in Model A. Moreover, Model B has a total harmonic distortion (THD) of 16.81%, which is lower than the 29.44% in Model A for the fundamental wave of magnetic flux density. In general, only the fundamental component of the magnetic flux density wave contributes to magnetic torque, while the harmonic components only increase iron loss.

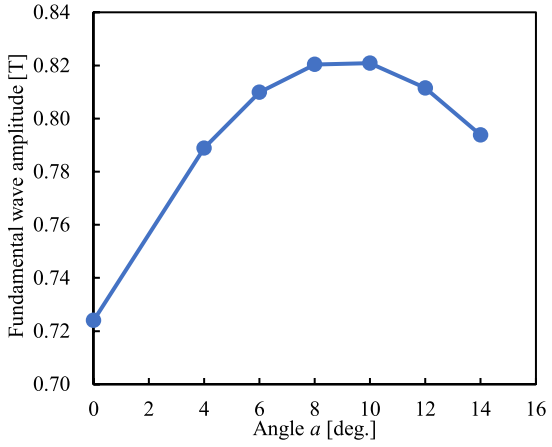

FIGURE 6. Fundamental wave amplitude of magnetic flux density observed in the airgap with the variation of angle a.

To determine the most optimum angle a, Fig. 6 shows the fundamental wave amplitude of magnetic flux density

observed in the airgap with the variation of angle a. As shown in the figure, when the angle a is less than or equal to 8 deg., the PM magnetic flux density is gradually concentrated by the large flux barriers with the increase of angle a. Therefore, the fundamental wave amplitude increases as angle a increases. However, when angle a is greater than or equal to 10 deg., the fundamental wave amplitude decreases as angle a increases due to the magnetic saturation between the flux barriers. Moreover, the fundamental wave amplitudes at $a = 8$ deg. and $a = 10$ deg. are very similar. Furthermore, the torque of an IPMSM can be divided into magnetic torque and reluctance torque. Although the large flux barriers can increase the fundamental wave amplitude of magnetic flux density (which is also referred to as PM magnetic flux density for brevity), the q-axis magnetic flux path will be narrow at the same time. Fig. 7 shows the magnitudes of magnetic torque and reluctance torque with the variation of angle a. In this figure, a maximum torque control strategy has been adopted to generate the maximum torque while maintaining the same load current for all angles a. Model A has a torque of 1.6 Nm at 4000 rpm, with its reluctance torque being the largest and the magnetic torque being the smallest. As angle a increases, the q-axis magnetic flux path gradually becomes narrower. As a result, as angle a increases, the q-axis inductance (L_q) decreases, which causes the reluctance torque to decrease. Moreover, the magnitude of magnetic torque shown in Fig. 7 shows the same changing trends as the fundamental wave amplitude shown in Fig. 6. The magnetic torque has a maximum magnitude at either $a = 8$ deg. or $a = 10$ deg., which is 1.68 Nm. Considering the magnitude of the reluctance torque, the torque reaches a maximum magnitude at either $a = 6$ deg. or $a = 8$ deg.

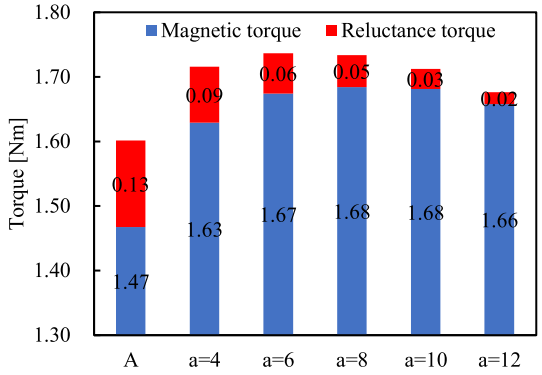

FIGURE 7. Magnitudes of magnetic torque and reluctance torque with the variation of angle a.

Fig. 8 shows copper loss and efficiency with the variation of angle a at operating point II. When angle a is less than or equal to 8 deg., the copper loss decreases as angle a increases because the magnetic torque increases. However, when angle a is greater than or equal to 8 deg., the copper loss increases as angle a increases because the magnetic torque does not increase while the reluctance torque decreases. When $a = 8$ deg., the efficiency reaches a maximum value at operating point II, which is 93.49%. Therefore, the model whose relative opening angle $a = 8$ deg. is chosen for Model B.

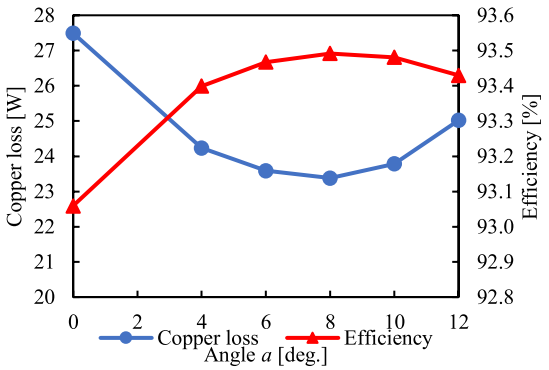

FIGURE 8. Copper loss and efficiency with the variation of angle a at operating point II.

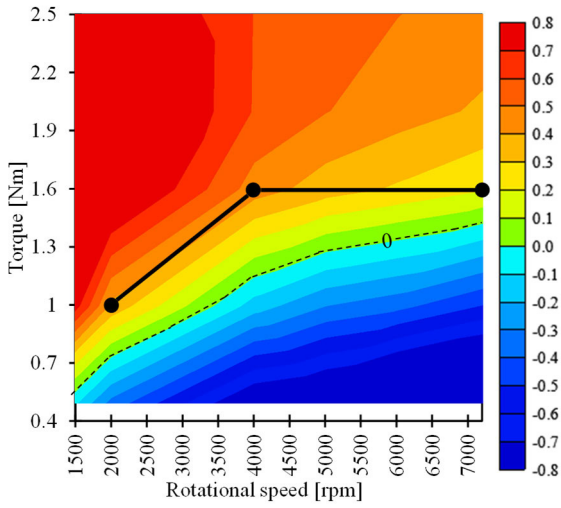

FIGURE 9. Efficiency difference map obtained by η_B - η_A.

Fig. 9 shows the efficiency difference map obtained by subtracting the efficiency of Model A from that of Model B (η_B - η_A). Over the entire target operating line, Model B is more efficient than Model A. Especially at operating point II, the copper loss of Model B is 23.38 W, which is 14.97% lower than the 27.50 W in Model A. As a result, the efficiency of Model B is 93.49%, which is 0.43% higher than the 93.06% in Model A. Moreover, the top-left side of the figure is a low-speed high-torque operating area while the bottom-right side is a high-speed low-torque operating area. Because copper loss is dominant in the low-speed high-torque operating area, the efficiency of Model B has been significantly enhanced. However, the efficiency of Model B is lower than that of Model A in the high-speed low-torque operating area.

To clarify the reason why the efficiency of Model B is lower than that of Model A at the high-speed low-torque operating area, Fig. 10 shows losses with the variation of torque at 7200 rpm. Because the magnetic torque in Model B has been utilized effectively, as can be seen from Fig. 10(a), the copper loss of Model B is smaller than that of Model A

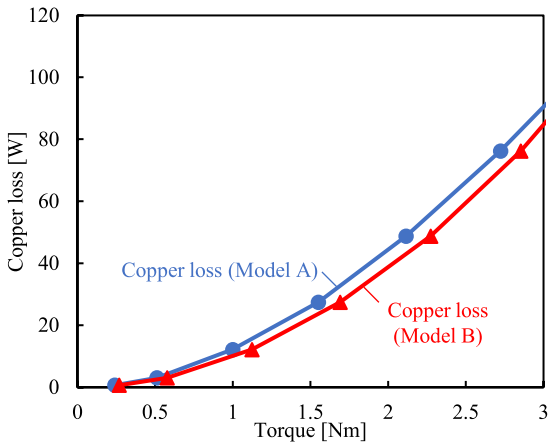

(a) Copper loss

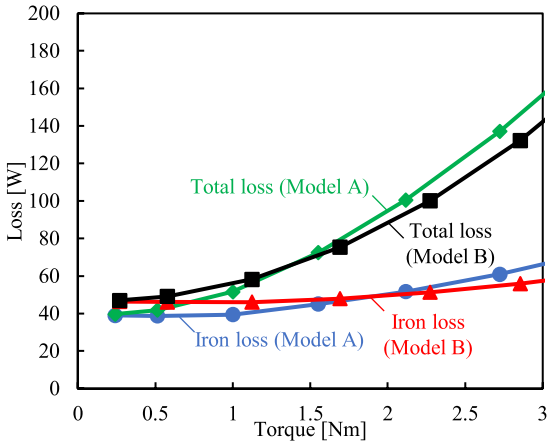

(b) Iron and total losses

FIGURE 10. Losses with the variation of torque at 7200 rpm.

throughout the entire operating line of 7200 rpm. The iron and total losses with the variation of torque at 7200 rpm are shown in Fig. 10(b). Iron losses do not change as drastically as copper losses because the torque increases while the rotational speed remains at 7200 rpm. Moreover, the iron loss of Model B is larger than that of Model A at the low-torque operating area, but smaller than that of Model A at the high-torque operating area. As a result, although the copper loss of Model B is smaller than that of Model A throughout the entire operating line of 7200 rpm, considering the iron loss, the total loss of Model B is larger than that of Model A at the low-torque operating area, but smaller than that of Model A at the high-torque operating area.

Fig. 10 shows the losses at load, to further disassemble iron loss, Fig. 11 shows the spectrum of iron loss of Models A and B at 7200 rpm and no load. The iron loss component with the same frequency as the drive frequency is referred to as the fundamental iron loss component. Therefore, if the abscissa is 1, it means that the frequency of this iron loss component is the fundamental component which has the same frequency as the drive frequency. If the abscissa is 2, it means that the frequency of this iron loss component is 2 times the drive frequency, and so on. The iron loss harmonic components of

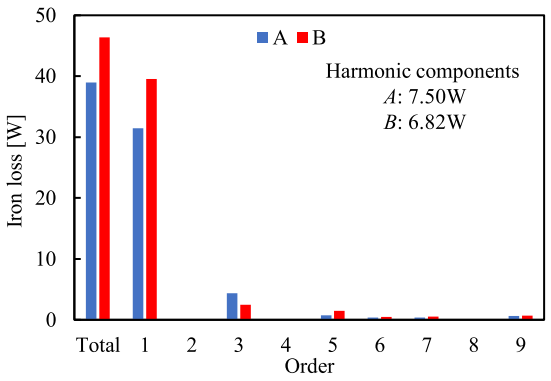

FIGURE 11. Spectrum of iron loss at 7200 rpm and no load.

Model B are 6.82 W, which is smaller than that the 7.50 W in Model A. However, the iron loss fundamental component of Model B is larger than that of Model A, which is the reason why the iron loss of Model B is larger than that of Model A at the low-torque operating area.

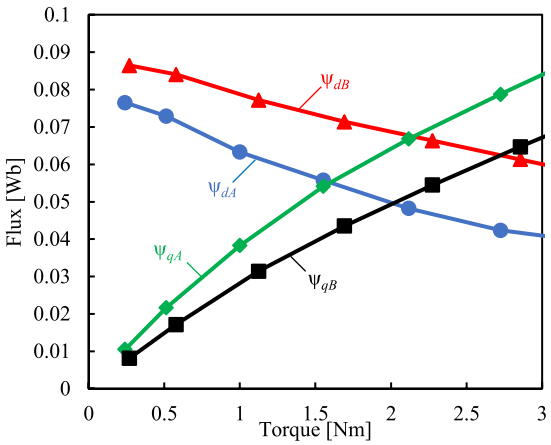

(a) *D*-axis magnetic flux (ψ_d) and *q*-axis magnetic flux (ψ_q)

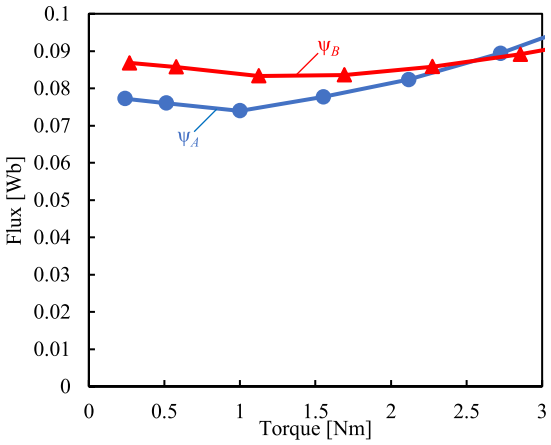

(b) Total Magnetic flux (ψ)

FIGURE 12. Magnetic flux with the variation of torque at 7200 rpm.

Fig. 12 shows the magnetic flux of Models A and B with the variation of torque at 7200 rpm. As shown in Fig. 12(a), the d-axis magnetic flux (ψ_d) of Model B is larger than that of Model A throughout the entire operating line of 7200 rpm

because of its larger PM magnetic flux density. Moreover, the q-axis magnetic flux (ψ_q) of Model B is smaller than that of Model A throughout the entire operating line of 7200 rpm because of its narrower q-axis magnetic flux path. The load current and its phase angle are small at the low-torque operating area. Therefore, the total magnetic flux (ψ) can be considered as being entirely generated by the d-axis magnetic flux. The total magnetic flux of Model B is larger than that of Model A because of its larger d-axis magnetic flux. With torque increases, the load current and its phase angle also increase. As a result, the q-axis magnetic flux increases while the d-axis magnetic flux decreases. As shown in Fig. 12(b), when the large q-axis magnetic flux of Model A is considered, the total magnetic flux of Model B becomes smaller than that of Model A at the high-torque operating area.

As mentioned above, adopting large flux barriers can reduce the copper loss of Model B because the PM magnetic flux can be concentrated on the d-axis and the utilization of magnetic torque can be improved. The large PM magnetic flux density, on the other hand, also causes an increase in total magnetic flux, which increases the iron loss fundamental component, particularly at the high-speed low-torque operating area.

IV. INVESTIGATION OF ROTOR STRUCTURE WHICH FOCUSES ON MINIMIZING IRON LOSS

Adopting large flux barriers has been discussed in the previous chapter to enhance efficiency by reducing copper loss. However, the large PM magnetic flux density also causes an increase in iron loss, particularly at the high-speed low-torque operating area. Considering either copper or iron losses should be reduced for the target operating line, this chapter proposes a rotor adopting a disproportional airgap to reduce iron loss by making the waveform closer to a sine wave.

As mentioned in the previous chapter, only the fundamental component of the magnetic flux density wave shown in Fig. 5 contributes to magnetic torque, while the harmonic components only increase iron loss. Therefore, this chapter focuses on reducing the harmonic iron components while maintaining the PM magnetic flux density unchanged.

Fig. 13 shows the rotor structure and its sketch for Model C, respectively. Compared with Model A, there is a disproportional airgap on q-axis magnetic flux path which can suppress q-axis magnetic flux and the harmonic components of dq-axis magnetic flux. Because the magnetoresistance of air is much larger than that of ferromagnetic material, a long airgap will lead to a reduction in PM magnetic flux density. Therefore, to ensure the PM magnetic flux density does not decrease, as shown in Fig. 13(b), a segment of the arc of Model A has been reserved. The blue arc is connected to Model A's arc, and the green line is tangent to the blue line. Length d is defined as the length of the disproportional airgap.

Fig. 14 shows the magnetic flux density waveforms of Models A and C ($d = 1.3$ mm) observed in the airgap. The

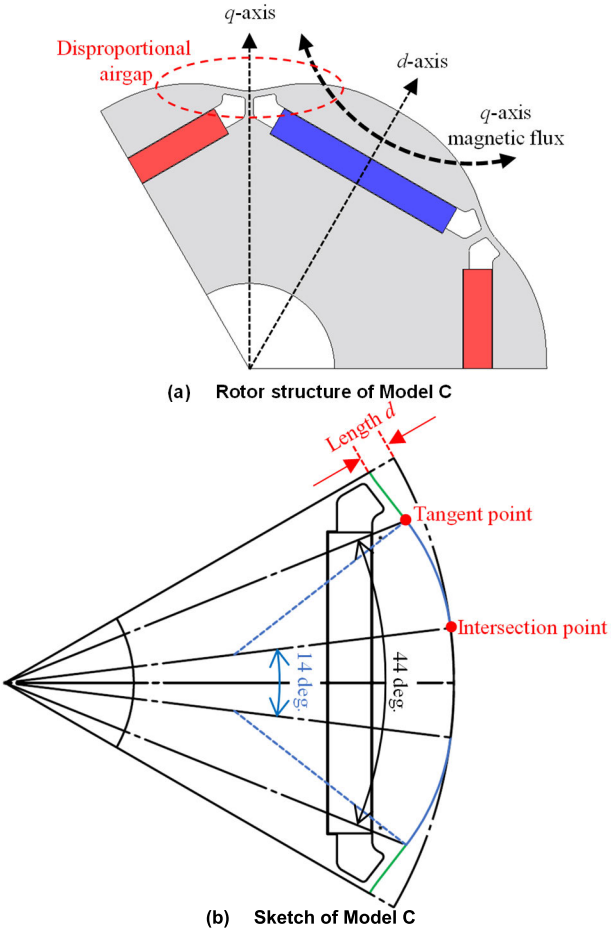

FIGURE 13. Rotor structure and its sketch for Model C.

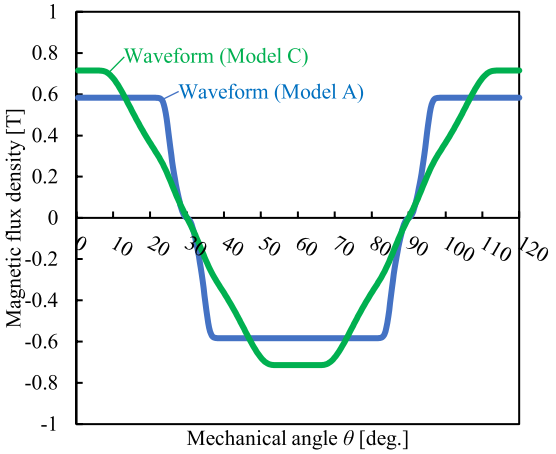

FIGURE 14. Magnetic flux density waveforms observed in the airgap.

observation method is the same as in Model B, as shown in Fig. 4. The waveform of Model C ($d = 1.3$ mm) is close to a sine wave in comparison to the waveform of Model A, which is close to a rectangular wave.

To determine the optimum disproportional airgap length d. Fig. 15 shows the fundamental wave amplitude and their THD of the magnetic flux density observed in the airgap with the variation of length d. The fundamental wave amplitude

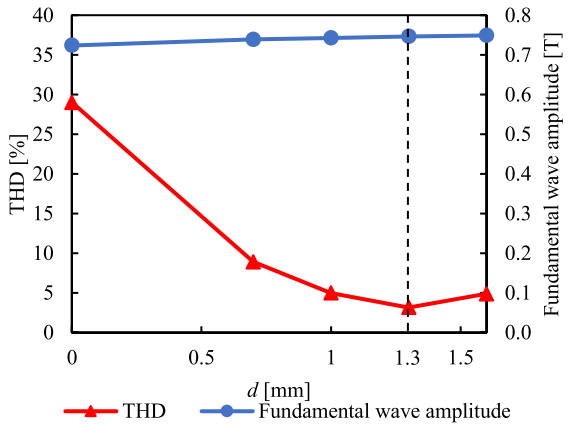

FIGURE 15. Fundamental wave amplitude and their THD of the magnetic flux density observed in the airgap with the variation of length *d*.

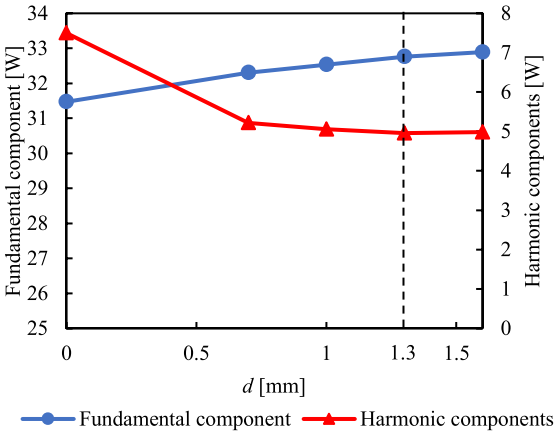

FIGURE 16. Fundamental and harmonic components of iron loss with the variation of length *d* at 7200 rpm and no load.

increases slightly with length d increases. At the same time, the THD decreases first and then increases, and reaches a minimum value when $d = 1.3$ mm. Fig. 16 shows the fundamental and harmonic components of iron loss with the variation of length d at 7200 rpm and no load. As a result, the iron loss fundamental component increases slightly as length d increases. And when length d is less than or equal to 1.3 mm, the iron loss harmonic components decrease as the length d increases. When length d is greater than or equal to 1.3 mm, the iron loss harmonic components remain nearly unchanged. Therefore, the model whose disproportional length $d = 1.3$mm is chosen for Model C.

Fig. 17 shows the iron loss spectrum of Models A and C at 7200 rpm and no load. The iron loss fundamental component of Model C is slightly larger than that of Model A due to its slightly larger PM magnetic flux density. However, the iron loss harmonic components of Model C decrease significantly. As a result, the iron loss of Model C is smaller than that of Model A. Moreover, Fig. 18 shows the q-axis magnetic flux waveforms of Models A and C at operating point II. Compared with Model A, the fundamental component of q-axis magnetic flux in Model C is 21.32% lower. As mentioned in the previous chapter, a decrease in q-axis magnetic flux

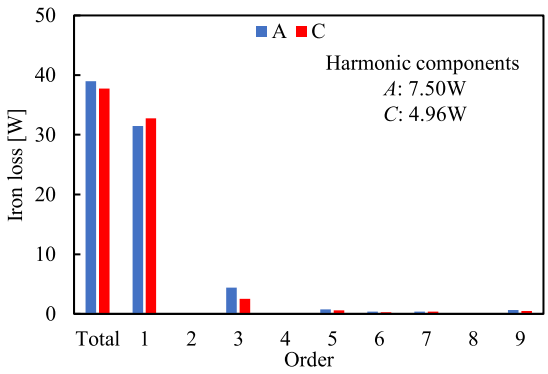

FIGURE 17. Spectrum of iron loss at 7200 rpm and no load.

results in a decrease in total magnetic flux, which can reduce iron loss. Furthermore, compared with Model A, Model C suppresses the 6th harmonic component, which can suppress the 5th and 7th iron loss.

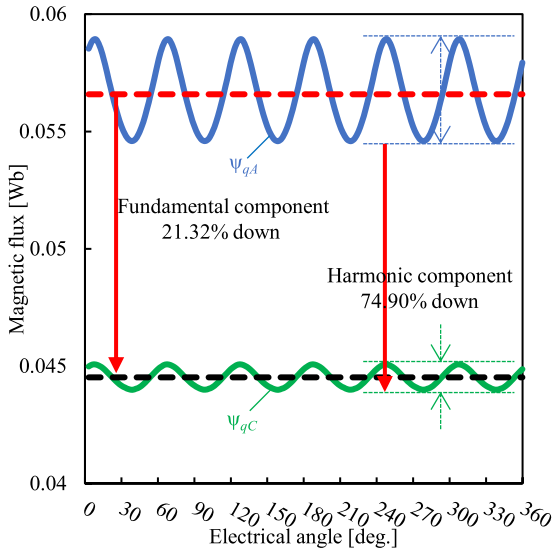

FIGURE 18. *Q*-axis magnetic flux waveforms at operating point II.

Fig. 19 shows losses with the variation of torque at 7200 rpm. As shown in Fig. 19(a), the iron loss of Model C is smaller than that of Model A throughout the entire operating line of 7200 rpm. Moreover, Fig. 19(b) shows the total and copper losses. Same with adopting large flux barriers, the q-axis magnetic flux path in Model C also becomes narrower. As a result, compared with Model A, the reluctance torque of Model C is smaller at the same operating point, resulting in an increase in copper loss. Therefore, the copper loss of Model C is slightly smaller than that of Model A at the very low-torque operating area due to its slightly larger PM magnetic flux density. However, because magnetic saturation is basically nonexistent, reluctance torque increases as load current and its angle increase. As a result, because the reluctance torque of Model C is smaller at the same operating point, its copper loss increases faster than that of model A when torque increases. Considering iron loss should be emphasized at this operating line of 7200 rpm due to high

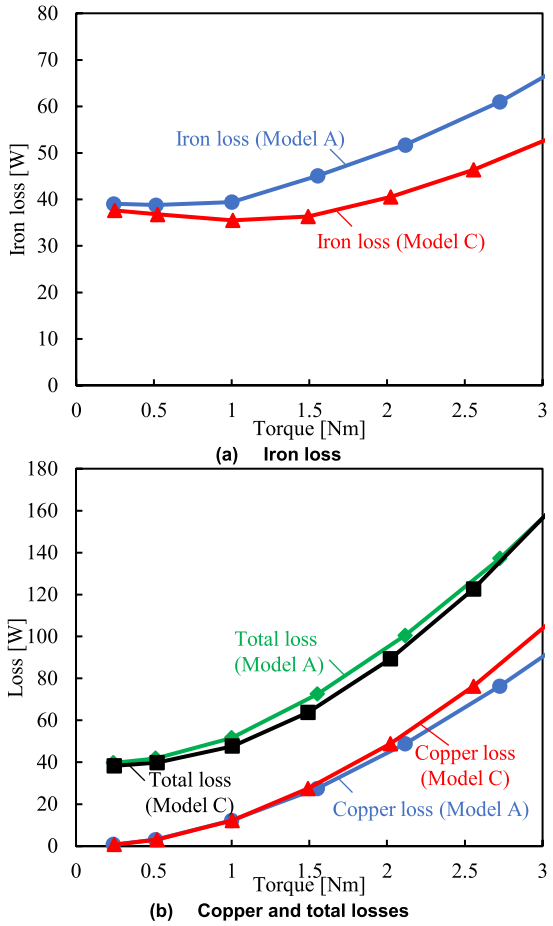

FIGURE 19. Losses with the variation of torque at 7200 rpm.

rotational speed, Model C has a smaller total loss than that of Model A throughout the entire operating line of 7200 rpm because of its smaller iron loss.

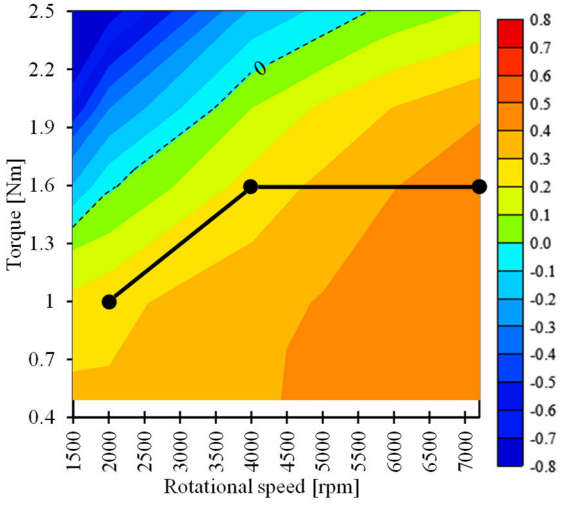

FIGURE 20. Efficiency difference map obtained by η_C - η_A.

Fig. 20 shows the efficiency difference map obtained by subtracting the efficiency of Model A from that of Model C (η_C- η_A). Same with Model B, Model C is also more efficient than Model A over the entire target operating line. Especially at operating point III, the iron loss of Model C is 37.00 W, which is 17.31% lower than the 44.75 W in Model A. As a result, the efficiency of Model C is 94.64%, which is 0.46% higher than the 94.18% in Model A. Moreover, because iron loss is dominant in the high-speed low-torque operating area, the efficiency of Model C has been significantly enhanced.

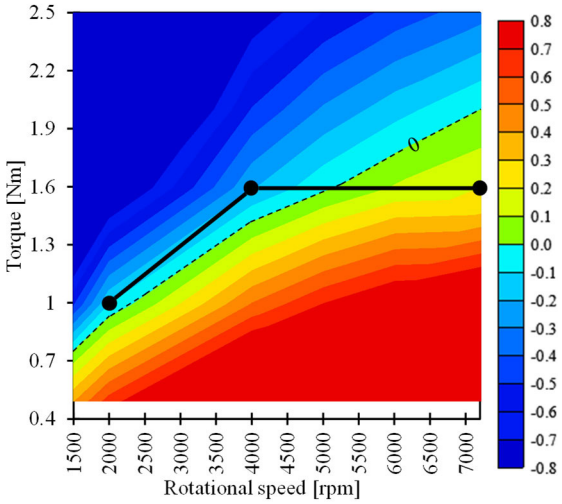

FIGURE 21. Efficiency difference map obtained by $\eta_C - \eta_B$.

Fig. 21 shows the efficiency difference map obtained by subtracting the efficiency of Model B from that of Model C ($\eta_C - \eta_B$). At operating point III, the iron losses of Model B and C are 47.55 W and 37.00 W, respectively. As a result of a smaller iron loss, the efficiency of Model C is 0.29% larger. However, when the operating point is changed from III to II, the torque remains constant at 1.6 Nm while rotational speed decreases. Therefore, copper loss does not change drastically as iron loss does. The iron loss of Model C decreases from 37.00 W at operating point III to 19.04 W at operating point II, while the copper loss only decreases from 31.54 W to 29.14 W. The copper and iron losses of Model B are 23.38 W and 23.21 W at operating point II, respectively. Although the iron loss of Model C is still smaller than that of Model B, copper loss should be emphasized at operating point II. As a result of a smaller copper loss, the efficiency of Model B is 0.19% higher than that of Model C at operating point II.

Fig. 22 shows the comparison of efficiency over the entire operating area. The efficiency of Model B is the highest in operating areas E and F, where copper loss should be emphasized. While the efficiency of Model C is the highest at operating areas G and H, where iron loss should be emphasized. Moreover, although the efficiency of both Models B and C is higher than that of Model A over the entire target operating line, Model B is more efficient at operating point II, while the Model C is more efficient at operating point III.

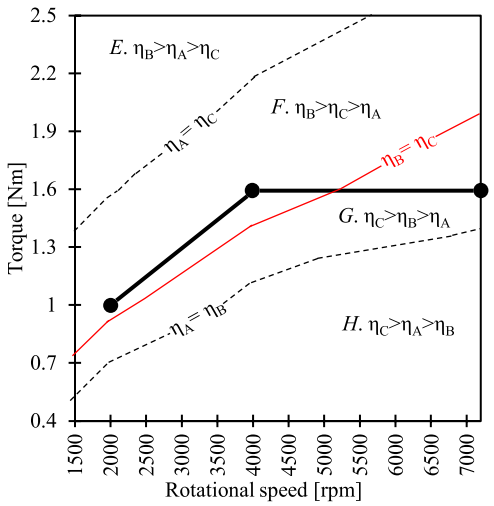

FIGURE 22. Comparison of efficiency over entire operating area.

V. INVESTIGATION OF ROTOR STRUCTURE THAT CAN TAKE ADVANTAGE OF BOTH ROTORS B AND C

In chapters III and IV, Model B can reduce copper loss by adopting large flux barriers to concentrate the magnetic flux of PMs on d-axis while suppressing q-axis magnetic flux. And Model C can reduce iron loss by adopting a disproportional airgap to suppress q-axis magnetic flux and the harmonic components of dq-axis magnetic flux. To take advantage of both Models B and C for further enhancing efficiency on the target operating line, a novel rotor structure is proposed in this chapter.

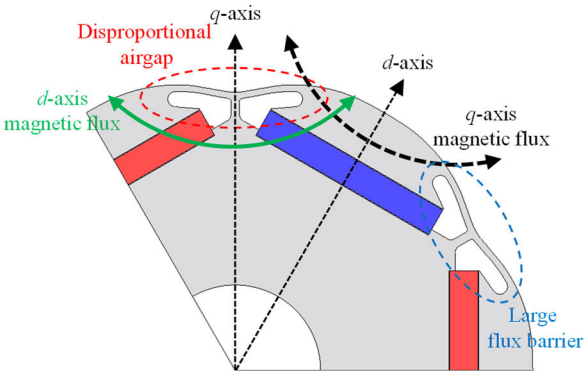

FIGURE 23. Rotor structure of model D.

TABLE 2. Fundamental wave amplitudes and their THDs of the magnetic flux density waveforms.

	A	B	C	D
Fundamental wave amplitude [T]	0.724	0.820	0.747	0.808
THD [%]	29.44	16.81	3.18	14.30

Fig. 23 shows the rotor structure of Model D. There are both large flux barriers and a disproportional airgap on q-axis magnetic flux path to concentrate the magnetic flux of PMs on d-axis while suppressing q-axis magnetic flux and the harmonic components of dq-axis magnetic flux in this model.

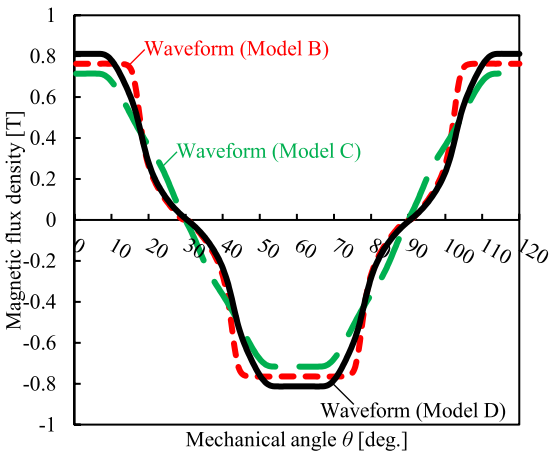

FIGURE 24. Magnetic flux density waveforms observed in the airgap.

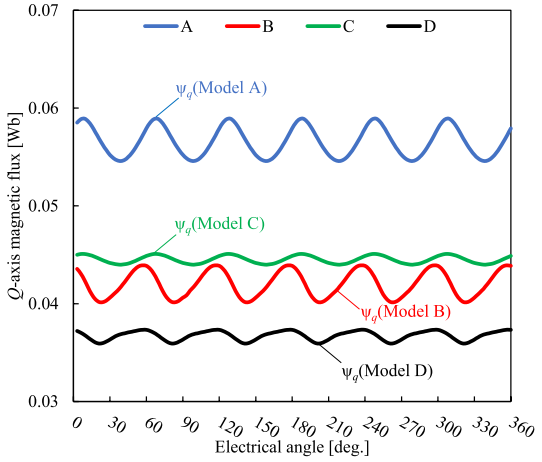

FIGURE 25. Q-axis magnetic flux waveforms at operating point II.

Fig. 24 shows the magnetic flux density waveforms of Models B, C and D observed in the airgap. The observation method is the same as in Model B, as shown in Fig. 4. Table 2 shows the fundamental wave amplitudes and their THDs of the magnetic flux density waveforms shown in Fig. 24. The fundamental wave amplitude of Model D is 0.808 T, which is 1.52% lower than the 0.820 T in Model B and 8.20% higher than the 0.747 T in Model C. Moreover, the THD of Model D is 14.30%, which is smaller than the 16.81% in Model B and higher than the 3.18% in Model C. Furthermore, Fig. 25 shows the q-axis magnetic flux waveforms of Models B, C and D at operating point II. The fundamental component of q-axis magnetic flux in Model D is the smallest because of its narrowest q-axis magnetic flux path. Therefore, iron loss can be suppressed in Model D by suppressing q-axis magnetic flux, as discussed in Chapter III.

As a result, Model D can reduce copper loss by effectively utilizing magnetic torque, and iron loss by suppressing q-axis magnetic flux.

Fig. 26 shows the efficiency difference map obtained by subtracting the efficiency of Model B from that of Model D ($\eta_D - \eta_B$). Model D has a slightly smaller PM magnetic flux density than Model B, and the q-axis magnetic flux has been

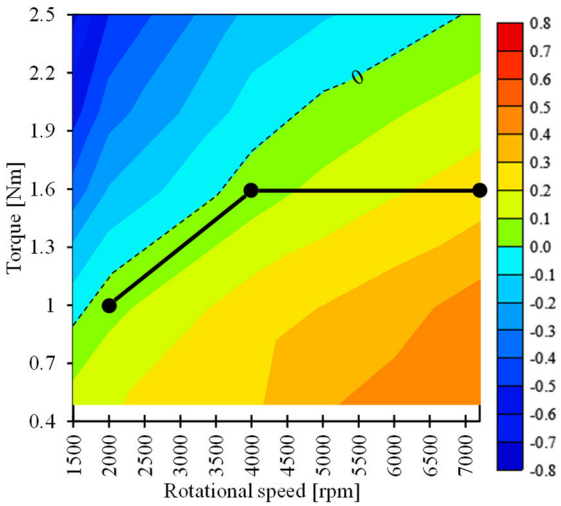

FIGURE 26. Efficiency difference map obtained by $\eta_D - \eta_B$.

effectively suppressed, resulting in an increase in copper loss and a decrease in iron loss. As a result, the efficiency of Model D is slightly higher than that of Model B at operating points I and II, and higher than Model B at operating point III.

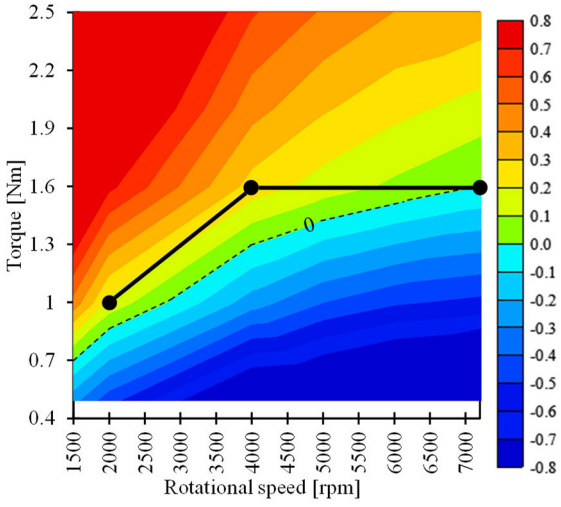

FIGURE 27. Efficiency difference map obtained by $\eta_D - \eta_C$.

Fig. 27 shows the efficiency difference map obtained by subtracting the efficiency of Model C from that of Model D ($\eta_D - \eta_C$). Model D has a larger PM magnetic flux density than Model C, resulting in an increase in iron loss and a decrease in copper loss. And a smaller q-axis magnetic flux, which can suppress iron loss. As a result, the efficiency of Model D is nearly equal to that of Model C at operating point III, but higher at operating points I and II.

Fig. 28 shows the comparison of the efficiency of Models B, and D over the entire operating area. The copper loss is dominant in operating area E. Therefore, Model B has the highest efficiency in this operating area because of its

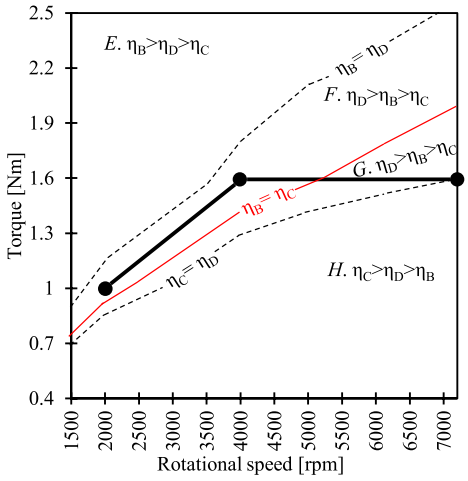

FIGURE 28. Comparison of efficiency over the entire operating area.

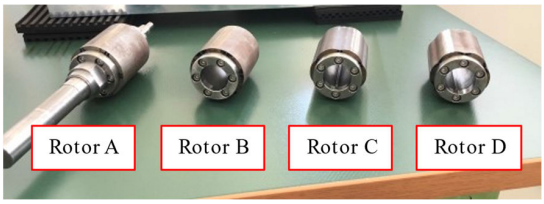

(a) Appearance of the four rotors

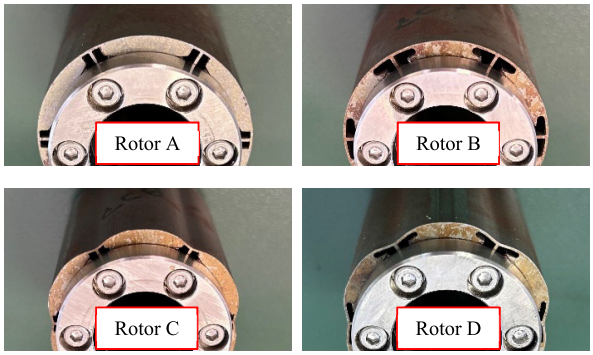

(b) Enlarged views of the four rotors

FIGURE 29. Appearance and enlarged views of the four rotors.

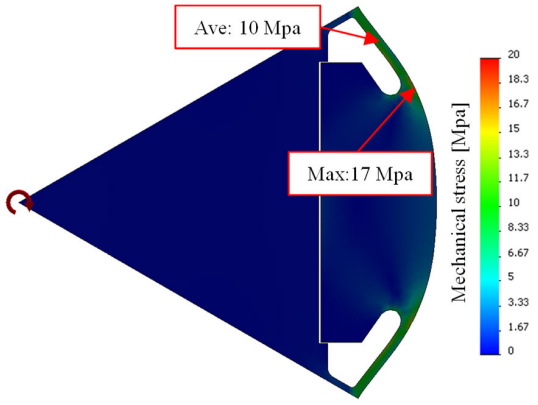

FIGURE 30. Mechanical stress distribution of model D.

largest PM magnetic flux density, implying that the magnetic torque was utilized most effectively. The iron loss is dominant

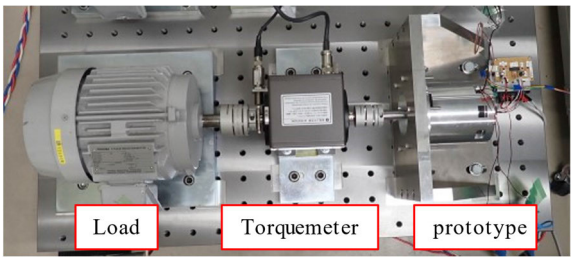

(a) Platform and prototype

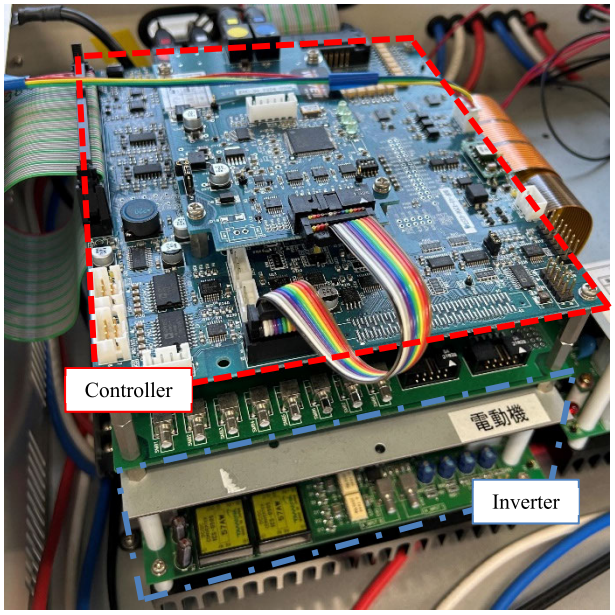

(b) Digital controller and inverter

(c) Power meter

FIGURE 31. Appearance of measure and drive devices.

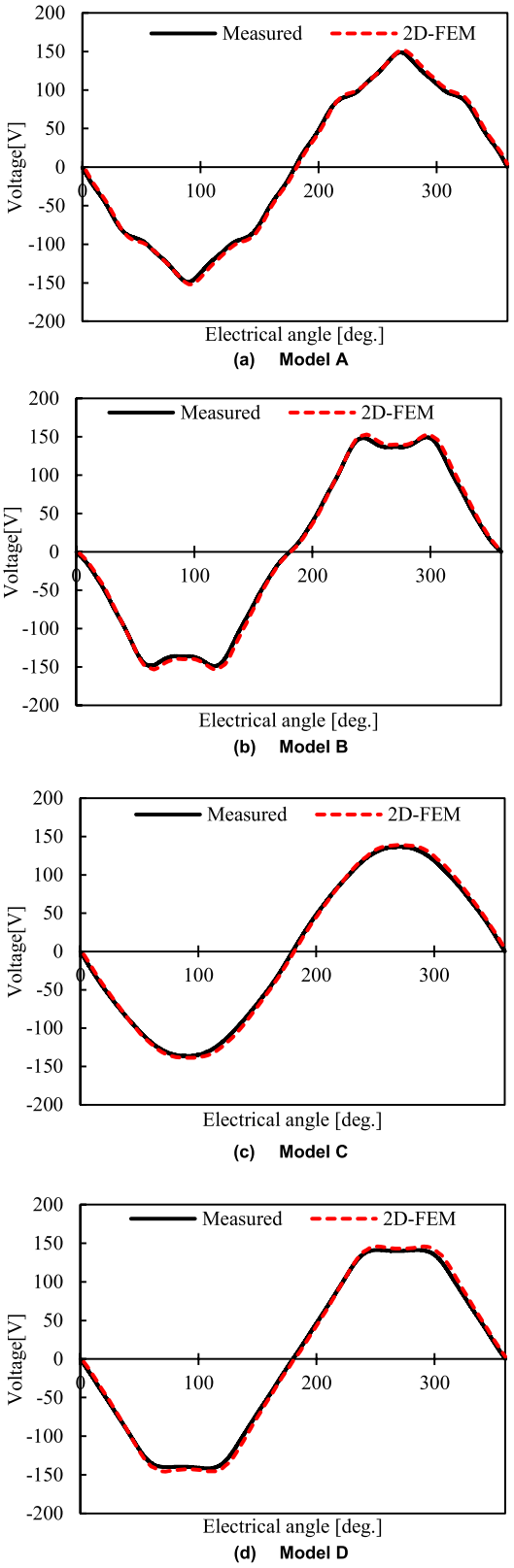

FIGURE 32. Back electromotive forces (b-EMFs) of the four models at 4000 rpm.

in operating area H. Therefore, Model C has the highest efficiency in this operating area because its PM magnetic flux density is small, and the q-axis and the harmonic components of dq-axis magnetic flux were suppressed. The efficiency of Model D is the highest at operating points F and G because the magnetic torque was utilized effectively, and the q-axis magnetic flux is the smallest, while the harmonic components of dq-axis magnetic flux were also suppressed. The iron loss of Model D is smaller than that of Model B, while the copper loss is smaller than that of Model C. As a result, Model D realized a tradeoff between copper and iron losses to minimize total loss, and has the highest efficiency at the target operating line.

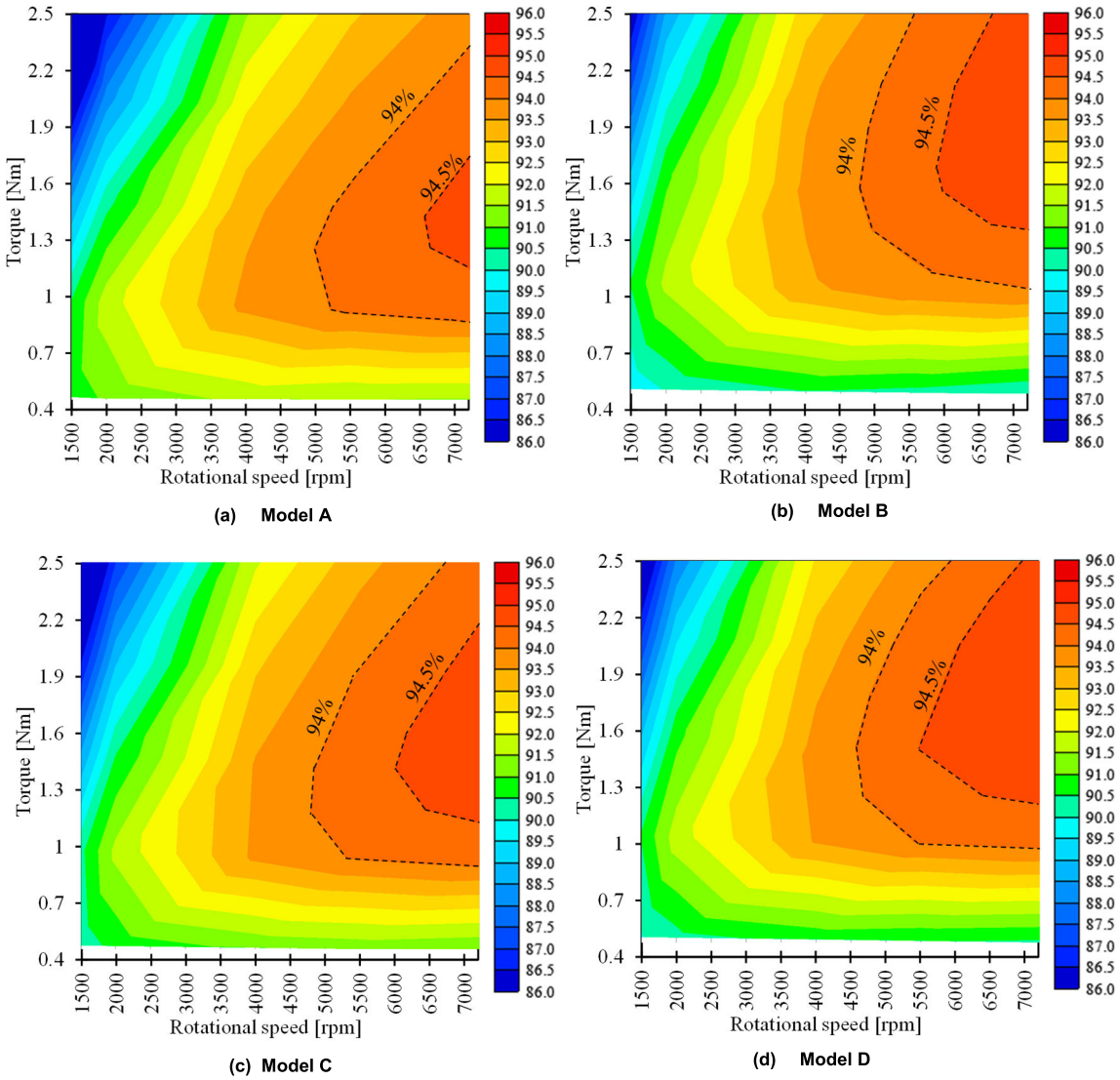

FIGURE 33. Measured efficiency map of the four models.

VI. EXPERIMENTAL VERIFICATION

A prototype machine is manufactured to verify the 2D-FEM results. Fig. 29 shows the appearance and enlarged views of the four rotors. To ensure the experimental accuracy, the rotors can be disassembled from the shaft while the same shaft is being used. The mechanical stress distribution of Model D is shown in Fig. 30. Because the diameter of the rotor is 41.8 mm, and the maximum rotational speed is 7200 rpm, the max mechanical stress for Model D is only 17 Mpa, which is sufficient for the 278 Mpa yield strength of the electrical steel used in the prototype.

Fig. 31 shows the appearance of the measure and drive devices. Fig. 31(a) shows the test platform and the prototype. The digital controller and inverter are shown in Fig. 31(b), and the power meter, which model is YOKOGAWA WT1804E, is shown in Fig. 31(c).

Fig. 32 shows the back electromotive forces (b-EMFs) of the four models at 4000 rpm. The measured waveforms of the four models, as shown in the figure, well matched the 2D-FEM analytical results. It should be noted that the waveform of Model C is close to an ideal sine wave. In general, the iron loss is considered to be reduced when the b-EMF voltage is closer to a sine wave. In fact, Model C always has the smallest iron loss. However, Model D has the highest efficiency for the target operating area because not only iron loss, but also copper loss should be considered.

Fig. 33 shows the measured efficiency maps of the four models. The *dq*-axis current control strategy using PI (proportional-integral) controller is adopted. The highest efficiencies of the four models all higher than 94.5%. Moreover, among the four models, Model D has the widest operating area where efficiency is higher than 94.5%.

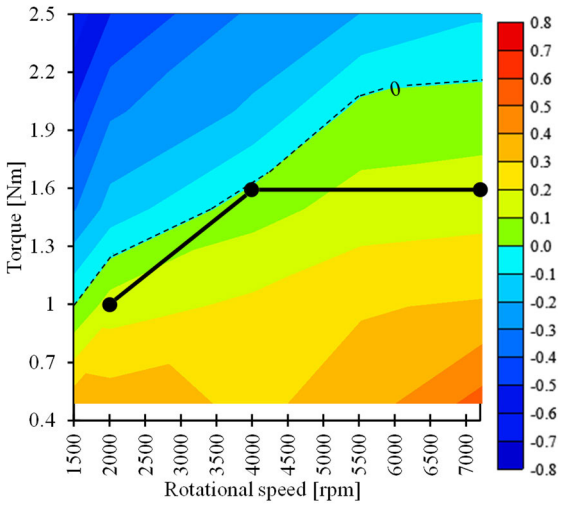

FIGURE 34. Measured efficiency difference map obtained by $\eta_D - \eta_B$.

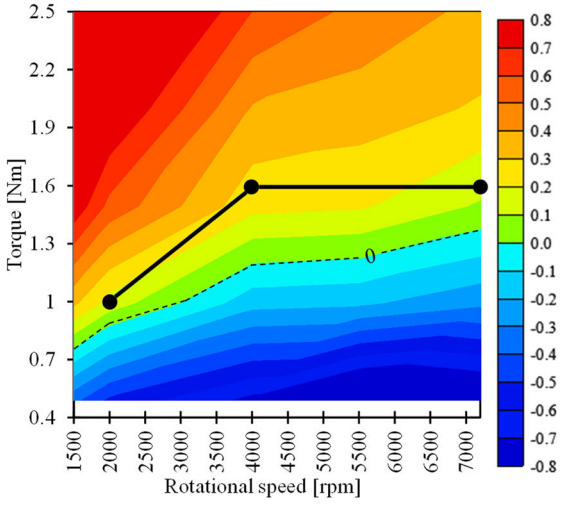

FIGURE 35. Measured efficiency difference map obtained by $\eta_D - \eta_C$.

Fig. 34 shows the measured efficiency difference map obtained by subtracting the efficiency of Model B from that of Model D ($\eta_D - \eta_B$). And Fig. 35 shows the measured efficiency difference map obtained by subtracting the efficiency of Model C from that of Model D ($\eta_D - \eta_C$). The efficiency of Model D is higher than that of both Models B and C at the target operating line. Moreover, Fig. 36 shows the comparison of the measured efficiency of Models B, C, and D over the entire operating area. The efficiency of Model D is highest at the target operating line. It should be noted that when compared to the 2D-FEM results, the operating area with the highest measured efficiency of Model D shifted slightly to the low-torque operating area because the proportion of copper loss in measured results is larger.

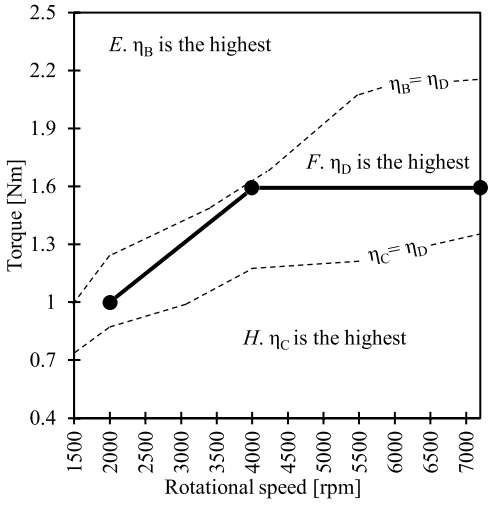

FIGURE 36. Comparison of the measured efficiency over the entire operating area.

VII. CONCLUSION

This paper proposed a novel rotor structure which can enhance efficiency at the target wide-speed middle-torque operating area without additional manufacturing costs. The proposed rotor structure employs both large flux barriers and a disproportional airgap on q-axis magnetic flux to concentrate the magnetic flux of PMs on d-axis while suppressing q-axis magnetic flux and the harmonic components of dq-axis magnetic flux. This paper first examined the effects of adopting large flux barriers and a disproportional airgap on utilization ratio of magnetic flux generated by PMs, the dimension of q-axis magnetic flux path, and the proportion of harmonic iron loss components, before examining their effects on copper and iron losses. As a result, the proposed rotor structure can reduce copper loss by effectively utilizing magnetic torque and iron loss by suppressing q-axis magnetic flux. A tradeoff between copper and iron losses has been realized in the proposed rotor structure to minimize total loss for the target operating line. Furthermore, this paper also clarified the design method for a suitable rotor structure depending on its target operating area. The results are as follows. For the target wide-speed middle-torque operating area, the proposed rotor structure is most suitable. For a low-speed high-torque operating area, adopting only large flux barriers is most suitable. And for a high-speed low-torque operating area, adopting only a disproportional airgap is most suitable. Finally, a prototype was manufactured to verify the results above.

REFERENCES

[1] J. Du, X. Wang, and H. Lv, "Optimization of magnet shape based on efficiency map of IPMSM for EVs," *IEEE Trans. Appl. Supercond.*, vol. 26, no. 7, pp. 1–7, Oct. 2016, doi: 10.1109/TASC.2016.2594834.

[2] L. Fang, J. W. Jung, J. P. Hong, and J. H. Lee, "Study on high-efficiency performance in interior permanent-magnet synchronous motor with double-layer PM design," *IEEE Trans. Magn.*, vol. 44, no. 11, pp. 4393–4396, Nov. 2008, doi: 10.1109/TMAG.2008.2002001.

[3] B. H. Lee, S. O. Kwon, T. Sun, J. P. Hong, G. H. Lee, and J. Hur, "Modeling of core loss resistance for $d-q$ equivalent circuit analysis of IPMSM considering harmonic linkage flux," *IEEE Trans. Magn.*, vol. 47, no. 5, pp. 1066–1069, May 2011, doi: 10.1109/TMAG.2010.2099647.
[4] H.-W. Lee, K. D. Lee, W. H. Kim, I. S. Jang, M. J. Kim, J. J. Lee, and J. Lee, "Parameter design of IPMSM with concentrated winding considering partial magnetic saturation," *IEEE Trans. Magn.*, vol. 47, no. 10, pp. 3653–3656, Oct. 2011, doi: 10.1109/TMAG.2011.2157957.
[5] R. Tsunata, M. Takemoto, S. Ogasawara, and K. Orikawa, "Variable flux memory motor employing double-layer delta-type PM arrangement and large flux barrier for traction applications," *IEEE Trans. Ind. Appl.*, vol. 57, no. 4, pp. 3545–3561, Jul. 2021, doi: 10.1109/TIA.2021.3068329.
[6] A. M. El-Refaie, J. P. Alexander, S. Galioto, P. B. Reddy, K. K. Huh, P. De Bock, and X. Shen, "Advanced high-power-density interior permanent magnet motor for traction applications," *IEEE Trans. Ind. Appl.*, vol. 50, no. 5, pp. 3235–3248, Sep. 2014, doi: 10.1109/TIA.2014.2305804.
[7] A. M. El-Refaie, "Fractional-slot concentrated-windings synchronous permanent magnet machines: Opportunities and challenges," *IEEE Trans. Ind. Electron.*, vol. 57, no. 1, pp. 107–121, Jan. 2010, doi: 10.1109/TIE.2009.2030211.
[8] M.-J. Kim, S.-Y. Cho, K.-D. Lee, J.-J. Lee, J.-H. Han, T.-C. Jeong, W.-H. Kim, D.-H. Koo, and J. Lee, "Torque density elevation in concentrated winding interior PM synchronous motor with minimized magnet volume," *IEEE Trans. Magn.*, vol. 49, no. 7, pp. 3334–3337, Jul. 2013, doi: 10.1109/TMAG.2013.2241747.
[9] Y. Fan, C. Tan, S. Chen, and M. Cheng, "Design and analysis of a new interior permanent magnet motor for EVs," in *Proc. IEEE 8th Int. Power Electron. Motion Control Conf. (IPEMC-ECCE Asia)*, May 2016, pp. 1357–1361, doi: 10.1109/IPEMC.2016.7512487.
[10] Y. Kano, T. Terahai, T. Kosaka, N. Matsui, and T. Nakanishi, "A new flux-barrier design of torque ripple reduction in saliency-based sensorless drive IPM motors for general industrial applications," in *Proc. IEEE Energy Convers. Congr. Expo.*, Sep. 2009, pp. 1939–1945, doi: 10.1109/ECCE.2009.5316493.
[11] Y. Xiao, Z.-Q. Zhu, J.-T. Chen, D. Wu, and L.-M. Gong, "A novel spoke-type asymmetric rotor interior PM machine," in *Proc. IEEE Energy Convers. Congr. Expo. (ECCE)*, Oct. 2020, pp. 4050–4057, doi: 10.1109/ECCE44975.2020.9236321.
[12] M. Cirani, S. Eriksson, and J. Thunberg, "Innovative design for flux leakage reduction in IPM machines," *IEEE Trans. Ind. Appl.*, vol. 50, no. 3, pp. 1847–1853, May 2014, doi: 10.1109/TIA.2013.2289969.
[13] H. Xu and J. Li, "A sleeve-free interior permanent magnet high speed motor with non-uniform airgap," in *Proc. IEEE Int. Electric Mach. Drives Conf. (IEMDC)*, May 2019, pp. 733–738, doi: 10.1109/IEMDC.2019.8785366.
[14] Z. Wu, Y. Fan, C. H. T. Lee, D. Gao, and K. Yu, "Vibration optimization of FSCW-IPM motor based on iron-core modification for electric vehicles," *IEEE Trans. Veh. Technol.*, vol. 69, no. 12, pp. 14834–14845, Dec. 2020, doi: 10.1109/TVT.2020.3041336.
[15] G. D. Donato, F. G. Capponi, G. A. Rivellini, and F. Caricchi, "Integral-slot versus fractional-slot concentrated-winding axial-flux permanent-magnet machines: Comparative design, FEA, and experimental tests," *IEEE Trans. Ind. Appl.*, vol. 48, no. 5, pp. 1487–1495, Sep. 2012, doi: 10.1109/TIA.2012.2210011.
[16] D. Wu and Z. Q. Zhu, "Influence of slot and pole number combinations on voltage distortion in surface-mounted permanent magnet machines with local magnetic saturation," *IEEE Trans. Energy Convers.*, vol. 30, no. 4, pp. 1460–1471, Dec. 2015, doi: 10.1109/TEC.2015.2436065.

XIANJI TAO was born in Shandong, China, in 1994. He received the B.S. degree from the School of Electrical Engineering, Wuhan University, Hubei, China, in 2016, and the M.S. degree from the Graduate School of Information Science and Technology, Hokkaido University, Sapporo, Japan, in 2019, where he is currently pursuing the Ph.D. degree.

MASATSUGU TAKEMOTO (Member, IEEE) was born in Tokyo, Japan, in 1972. He received the B.S. and M.S. degrees in electrical engineering from the Tokyo University of Science, Noda, Japan, in 1997 and 1999, respectively, and the Ph.D. degree in electrical engineering from the Tokyo Institute of Technology, Tokyo, in 2005.

In 1999, he joined the Department of Electrical Engineering, Tokyo Institute of Technology, as a Research Associate. In 2004, he joined the Department of Mechanical Systems Engineering, Musashi Institute of Technology, Tokyo, as a Research Associate, where he became a Lecturer, in 2005. In 2008, he joined the Graduate School of Information Science and Technology, Hokkaido University, Sapporo, as an Associate Professor. Since 2020, he has been with Okayama University, Okayama, Japan, where he is currently a Professor with the Graduate School of Natural Science and Technology. He is engaged in research on permanent magnet synchronous motors, axial gap motors, rare-earth-free motors, bearingless motors, and magnetic bearings. He is a member of the Institute of Electrical Engineers of Japan (IEEJ). He was a recipient of the Nagamori Award from the Nagamori Foundation, in 2017, the IEEJ Transaction Paper Award, in 2005, the Prize Paper Awards from the Electric Machines Committee of the IEEE Industry Applications Society, in 2011 and 2019, and the Prize Paper Award from the Electrical Machines Technical Committee of the IEEE Industrial Electronics Society, in 2018. He has served as a Secretary, a Vice-Chair, and a Chair for the IEEE IAS Japan Chapter, in 2008–2009, 2010–2011, and 2012–2013, respectively.

REN TSUNATA (Member, IEEE) was born in Miyagi, Japan, in 1992. He received the B.S., M.S., and Ph.D. degrees in electrical engineering from Hokkaido University, Hokkaido, Japan, in 2015, 2017, and 2021, respectively.

He was with Toyota Motor Corporation, Aichi, Japan, from 2017 to 2018. In 2021, he joined Okayama University, Okayama, Japan, as a Research Fellow. Since 2022, he has been an Assistant Professor with the Graduate School of Natural Science and Technology, Okayama University. His research interests include permanent magnet synchronous machines, variable flux motors, and axial flux machines. He is a member of the Institute of Electrical Engineers of Japan (IEEJ) and the Japan Society of Applied Electromagnetics and Machines (JSAEM). He was a recipient of the four IEEJ Excellent Presentation Awards, in 2017, 2020, and 2022, and the Incentive Award from JSAEM, in 2020.

SATOSHI OGASAWARA (Senior Member, IEEE) was born in Kagawa, Japan, in 1958. He received the B.S., M.S., and Ph.D. degrees in electrical engineering from the Nagaoka University of Technology, Niigata, Japan, in 1981, 1983, and 1990, respectively. From 1983 to 1992, he was a Research Associate at the Nagaoka University of Technology. From 1992 to 2003, he was with the Department of Electrical Engineering, Okayama University. From 2003 to 2007, he was with the Department of Electrical Engineering, Utsunomiya University, Utsunomiya, Japan. Since 2007, he has been a Professor with the Graduate School of Information Science and Technology, Hokkaido University. His research interests include ac motor drive systems and static power converters. He is a fellow of the IEEJ. He received the IEEE Power Electronics Society Prize Paper Award, in 1999, and the IEEE Industry Applications Society Committee Prize Paper Awards, in 1996, 1997, 2003, and 2010.